

Received 10 July 2024, accepted 4 September 2024, date of publication 12 September 2024, date of current version 2 October 2024.

Digital Object Identifier 10.1109/ACCESS.2024.3458915



RESEARCH ARTICLE

Contact Force Control of Robot Polishing System Based on Vision Control Algorithm

KAI LIU[®]

School of Electrical Engineering, Changzhou Vocational Institute of Mechatronic Technology, Changzhou 213164, China e-mail: czimtlk@163.com

This work was supported by the Qing Lan Project under Grant [2024]-2.

ABSTRACT In this study, an autonomous robotic polishing system leveraging sensor signal processing and control technology is developed. It utilizes a primary-secondary configuration with machine vision and force sensors for intelligent defect detection. The system processes force sensor data to obtain an accurate contact force assessment and performs precise polishing using proportional integral derivative and impedance-based control strategies. It supports remote teaching operator control and autonomous operation of intelligent polishing. Experimental results show that the maximum error between the measured and true values is 0.36 mm. In arc detection, the maximum measurement error between the measured and true values is 1.02mm, and the average error is 0.33mm. This level of accuracy is considered sufficient for the specific applications targeted in this study, such as precision manufacturing, where high accuracy is essential but variability in measurements can be adapted to within a certain range. In actual polishing experiments, the roughness values of the designed industrial robot on pipes and wood were $0.491 \, \mu m$ and $0.487 \, \mu m$, respectively. Most of the polishing of defective locations is completed. Overall, the designed automatic polishing industrial robot is effective and can be applied to polishing operation in industrial production.

INDEX TERMS Visual control algorithm, six-dimensional force sensor, industrial robots, polishing homework, measurement error.

I. INTRODUCTION

In modern manufacturing, the use of industrial robots has become the key to improving production efficiency and product quality. Especially in the polishing operation, the introduction of robots can significantly reduce the intensity of manual labor, while surpassing traditional manual operations in terms of consistency and precision. However, although industrial robotics technology has made great progress, existing systems still face a series of challenges in practical applications [1], [2], [3]. The research motivation stems from a deep understanding of the limitations of existing industrial robot polishing systems. Traditional robotic systems often rely on pre-programmed paths and simple tactile feedback when performing polishing tasks, which limits their ability to adapt to changes in the workpiece surface. For example, when there are irregularities or tiny defects on the workpiece

The associate editor coordinating the review of this manuscript and approving it for publication was Min Wang.

surface, traditional systems may not be able to accurately identify and adapt to these changes, resulting in uneven polishing quality. In addition, traditional systems also have deficiencies in controlling the precise application of polishing force, which directly affects the fineness and consistency of the polishing operation [4], [5]. The main difficulties include but are not limited to: accurate identification and location of surface defects on the workpiece, especially in the presence of complex geometries and diverse surface properties; difficulty in achieving precise control of the polishing force to maintain a constant contact force and adapt to different conditions; workpiece material and surface conditions; lack of autonomous learning and adaptability, leading to poor performance of robots in the face of unknown or changing working environments [6]. To overcome these difficulties and promote the development of industrial robot polishing technology, an autonomous polishing system based on machine vision control algorithm and six-dimensional force sensor is proposed. The system is designed to address the above



challenges by integrating advanced visual recognition technology and force control strategies to achieve intelligent detection of workpiece surface defects, precise positioning, and precise control of force and position during the polishing process. The innovation of the research is that by obtaining the surface morphology and position information of the workpiece in real time, combined with the feedback from the force sensor, the robot can plan the polishing path more flexibly and accurately to achieve high-quality polishing effects.

The research is divided into four parts. The first part is a summary and discussion of the current research on the automation control of polishing operations in polishing industrial robots. The second part is to design an industrial robot polishing control system using machine vision and the relevant force sensors. The third part is to verify the visual detection and polishing system in the system. The fourth part is a summary of the entire article.

II. RELATED WORKS

The polishing process is an essential part of industrial production, and is the key to ensuring product quality and controlling production costs. In the research of industrial robots, the automation control of polishing operations for industrial robots has always been a focus of many scholars [7], [8], [9]. Zhou et al. [10] proposed a novel control strategy to address the issue of smooth contact force in faucet polishing operations, which uses position control as the inner loop and tolerance control as the outer loop. To prevent excessive polishing, parameter sensitivity analysis was also introduced in the study. The study first established a system model, calculated parameter sensitivity, and analyzed the impact of allowable parameters on the system output. The position control and allowable control were verified through simulation, and the results showed that the new strategy can improve the position control accuracy by 3.0% and ensure that the contact force is close to the expected value. The polishing experiments conducted on industrial robots further confirmed the effectiveness of the control strategy, which can effectively control the contact force during the polishing process. In the field of industrial robot precision polishing, due to high mechanical rigidity, traditional robots are difficult to achieve perfect polishing. Li et al. [11] precisely controlled the contact force by installing an active compliant force control device at the end of the robot. However, the hysteresis non-linearity between cylinder air pressure and output force, as well as the random interference during the polishing process, may affect the accuracy of contact force, thereby affecting the polishing effect. To address this issue, a dRNN-PI model was designed to compensate for cylinder hysteresis non-linearity and calculate the air pressure required to maintain stable contact force. Meanwhile, the PSMC strategy is adopted to quickly track the required air pressure and avoid overshoot. The stability of the controller was verified through the Lyapunov method, and the experimental results confirmed the accuracy of the hysteresis compensation model and the effectiveness of PSMC. This study provides a new control strategy for improving the precision and stability of robot polishing, which helps to overcome cylinder hysteresis non-linearity and random interference, and achieve high-quality workpiece surface treatment. Ochoa and Cortesão [12] proposed a new impedance control (IC) method on the ground of the optimized end effector in industrial robot polishing IC, which effectively improved the effectiveness of robot polishing and enhanced the generalization of applications. Fan et al. [13] developed a novel adaptive belt tool system for precision machining of turbine blade blisks. A pneumatic servo system was adopted to control polishing force, and the nonlinear control of the pneumatic system was optimized through a two-dimensional fuzzy Proportional Integral Derivative (PID) controller. Compared with traditional PID, fuzzy PID controller significantly reduced steady-state error and overshoot. The experiment showed that the polishing process is stable and the roughness is controlled below 0.4 microns, which verifies the effectiveness of the new system and controller.

In addition, in robot machining, the accuracy of workpiece positioning is crucial for machining quality. Traditional control methods are difficult to achieve fast edge tracking and stable tool contact simultaneously. Therefore, Lloyd et al. [14] proposed the Simultaneous Registration and Machining (SRAM) framework, which combines force and position feedback to optimize workpiece positioning and path correction in real-time. SRAM can dynamically adjust controller damping based on positioning accuracy, quickly correct errors, and maintain machining stability. Through robot deburring testing verification, SRAM significantly reduced path and force tracking errors, improved machining quality, and reduced tool wear. This framework reduced the dependence on initial positioning accuracy, helped to reduce costs and shorten production cycles, and provided new ideas for the advancement of robot processing technology. Pan et al. [15] proposed a vibration suppression method for enhancing the damping ratio of the industrial robot polishing system, on the ground of dynamic modeling of the polishing system, to address the vibration impact problem. This effectively improved the quality of polishing processing while suppressing vibration. Ding et al. [16] proposed a parameter learning algorithm for IC of industrial robots by utilizing reinforcement learning to address the issue of maintaining the contact force stability of actuators in automatic polishing of industrial robots. This improved the stability of polishing contact force on the basis of predicting the distribution of output states. Accurate and stable force control is crucial for ensuring material removal rate and surface quality in robot grinding tasks. However, traditional methods are difficult to maintain constant force control due to various interfering factors. To address this challenge, Wu et al. [17] developed a dual PID adaptive variable impedance control (DPAVIC) strategy, which compensates for force errors through PD control, uses PID to update damping parameters to reduce interference, and uses a nonlinear tracking differentiator to smooth the expected force and reduce overshoot.

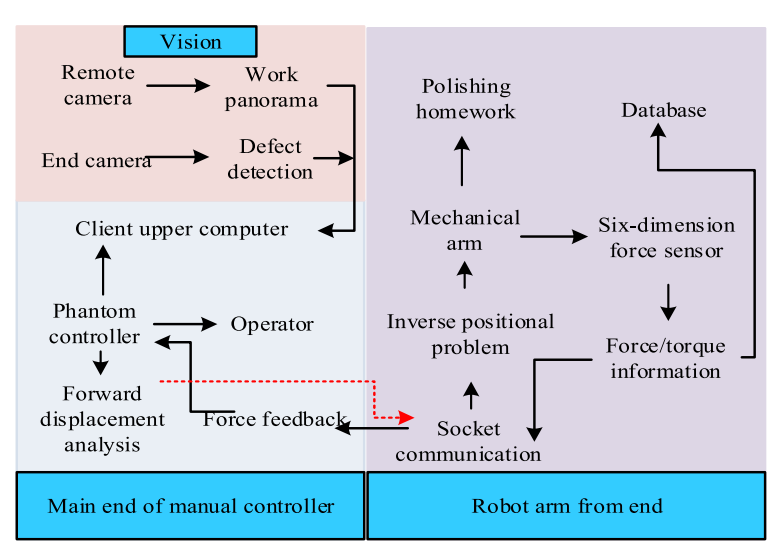


FIGURE 1. Schematic diagram of the remote sensing force feedback teaching polishing system framework.

The effectiveness of DPAVIC was verified through theoretical analysis, simulation, and experiments. Compared with CIC and AVIC, it significantly improved the force control accuracy in thin-walled workpiece grinding experiments, controlling the force tracking error within \pm 0.2 N and increasing the surface roughness to Ra 0.218 μ m. This indicated that DPAVIC provides an effective control strategy for precision robot polishing.

In the existing literature, although a variety of methods have been proposed for the automated control of industrial robot grinding operations, these studies mostly focus on grinding tasks under specific conditions, and have little regard for workpiece surface adaptability, force control accuracy, and grinding quality. There are limitations in consistency. To address these shortcomings, the study proposed an autonomous polishing system based on machine vision control algorithms and six-dimensional force sensors. The contribution of the research is: introducing a high-precision Mask Region-based Convolutional Neural Network (Mask R-CNN) to significantly improve the detection and positioning accuracy of workpiece surface defects; designing a polishing control strategy based on PID controller and positional IC to optimize the force and position during the polishing process precise control; constructing a primary-secondary system that integrates machine vision and force sensors, which enhanced the autonomy and adaptability of the system; verifying the effectiveness of the system through experiments, and demonstrating its potential in practical applications. These contributions not only promote the development of industrial robot polishing technology, but also provide new perspectives and methods for future research.

III. DESIGN AND CONTROL OF AN INDUSTRIAL ROBOT POLISHING SYSTEM WITH INTEGRATED VISION AND FORCE FEEDBACK

In the construction of the control structure module, the research integrated machine vision and six-dimensional force

sensor feedback to improve the accuracy and efficiency of industrial robot polishing. Capturing workpiece images through a high-precision camera system and using deep learning technology such as Mask R-CNN for defect identification can ensure accurate planning of the grinding path. At the same time, real-time processing of force sensor data provides the necessary force feedback for the control system, allowing the robot to dynamically adjust polishing parameters.

A. DESIGN OF ROBOT POLISHING SYSTEM BASED ON MACHINE VISION AND FORCE FEEDBACK

The research and design of a robot large-scale system using machine vision control algorithms and six-dimensional force sensors mainly consists of a primary-secondary system consisting of a vision system, a database, a hand controller, and a robotic arm. Therefore, the framework of the remote sensing force feedback teaching polishing system is shown in Figure 1.

Figure 1 shows that the main end of the controller includes a Phantom Premium 6-degree-of-freedom force feedback device, a client upper computer, and so on. The operator first calibrates the initial position of the hand controller and moves it, and obtains the terminal position of the operator's movement through forward kinematics solution. Simultaneously, the relative position deviation of the controller is transmitted to the robot server through Socket communication, and then the server controls the robot's actions on the ground of the position information. The function of the client personal computer is to provide visual, mechanical, and other information during the polishing process to the operator's hand and display it on the operator's arm, thereby improving the realism of the operation. In addition, the upper computer receives force and torque information from the six-dimensional force sensor, and controls the mechanical arm to output corresponding force and torque, enabling operators to perceive the tactile sensation during polishing processing. This can achieve force feedback-based remote control polishing. In the field



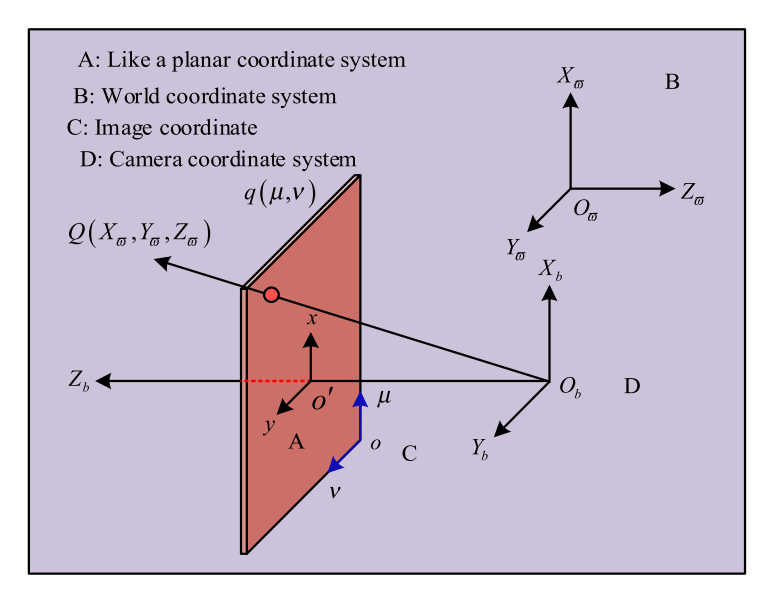


FIGURE 2. Schematic diagram of camera perspective projection model.

of industrial robot polishing, traditional technologies mainly include pre-programmed control methods, basic tactile feedback systems, non intelligent visual systems, open-loop control systems, single sensor applications, manual teaching methods, simple PID control strategies, non real-time data processing capabilities, and a lack of remote operation functions. These systems typically have low levels of automation, require manual monitoring and intervention, and have limitations in adapting to environmental changes and handling complex tasks. In contrast, the industrial robot autonomous polishing system proposed in the study achieves precise remote control of the robot by the operator by integrating a Phantom Advanced Edition 6-degree-of-freedom force feedback device and a six-dimensional force sensor. The system adopts forward kinematics and real-time Socket communication, ensuring the accuracy and flexibility of operation. The client computer provides visual and mechanical information feedback to the operator, enhancing the realism of the operation.

In the autonomous polishing vision system of industrial robots, traditional object detection and positioning have problems such as long time consumption and low accuracy, while the polishing process in industrial production also has defects such as size deviation and spot rust. Therefore, to solve these problems, the research first achieves precise positioning and size measurement of the workpiece by calibrating the camera. Secondly, the Mask R-CNN is utilized for locating the categories of defects, and the defects are semantically divided and accurately labeled to achieve automatic localization of grinding points. When industrial robots perform polishing processing, they first need to obtain visual information from the surrounding environment, then determine the specific position and defects of the processed object, and then control the polishing tool to a position close to the machining point. Therefore, it is essential for corresponding the spatial coordinates of the image to the real space Coordinate System (CS), which requires calibration of the camera and establishing corresponding relationships between each CS [18], [19], [20]. The concept of real space CS is crucial in automated polishing systems, as it ensures precise mapping of the robot to the actual position of the object. Calibrating the camera to the real space CS is crucial for integrating sensory data, performing precise mathematical transformations, ensuring operational consistency, and achieving multi-sensor data integration. Innovation is reflected in improving the accuracy and dynamism of calibration through advanced algorithms, as well as the ability to drive automation of complex tasks. Among them, the industrial robot vision system designed for research includes two cameras. The remote camera is installed in front of the robot arm to capture the actual polishing process, and the end camera is installed at the end of the robot arm for forming the hand eye system. The camera perspective projection model without considering lens distortion is shown in Figure 2.

In Figure 2, o, o', and O all represent the origin of the CS. $X_{\overline{w}}$, $Y_{\overline{w}}$ and $Z_{\overline{w}}$ represent the three-axis coordinates of the world CS. X_b , Y_b and Z_b represent the three-axis coordinates of the camera CS. x and y serve as the horizontal and vertical axes of the image plane CS. μ and ν represent the horizontal and vertical axes of the image CS. Q and q represent the camera matrix. Figure 1 shows that the perspective projection model includes the world CS, camera CS, image plane CS, and image CS. The function of the world CS is to reflect the actual spatial position of the camera and the object being measured. The origin of the camera CS is the optical center of the camera, and the z-axis coincides with the actual optical axis of the camera. Its purpose is for describing the position of objects from the camera [21], [22], [23]. The image plane CS is the plane on which the camera's photosensitive components image. The



image CS is the CS of the actual observable image, which can be regarded as a matrix. Each value in the matrix is the actual grayscale value of each pixel [24], [25], [26]. The transformation from the world CS to the camera CS is a rigid transformation of translation and rotation, as expressed in equation (1).

$$\begin{cases}
 \left[X_b \ Y_b \ Z_b \right]^T = \Re \left[X_{\varpi} \ Y_{\varpi} \ Z_{\varpi} \right]^T + L \\
 \Re \left(\psi, \gamma, \varphi \right) \begin{bmatrix} 1 & 0 & 0 \\ 0 & \cos \psi - \sin \psi \\ 0 & \sin \psi & \cos \psi \end{bmatrix} \begin{bmatrix} \cos \gamma & 0 & \sin \gamma \\ 0 & 1 & 0 \\ -\sin \gamma & 0 & \cos \gamma \end{bmatrix} \\
 \left[\begin{bmatrix} \cos \varphi - \sin \varphi & 0 \\ \sin \varphi & \cos \varphi & 0 \\ 0 & 0 & 1 \end{bmatrix} \\
 L = \begin{bmatrix} l_x \ l_y \ l_z \end{bmatrix}^T, \begin{bmatrix} X_b \ Y_b \ Z_b \ 1 \end{bmatrix}^T \\
 = \begin{bmatrix} \Re \ L \\ 0 \ 1 \end{bmatrix} \begin{bmatrix} X_{\varpi} \ Y_{\varpi} \ Z_{\varpi} \ 1 \end{bmatrix}
\end{cases}$$
(1)

In equation (1), \Re represents the rotation matrix. L represents the translation matrix, and l is its internal element. ψ represents pitch angle. γ represents yaw angle. φ represents the rolling angle. The second equation in the third row of equation (1) is the homogeneous coordinate form of the transformation formula. The camera CS converts coordinate points in three-dimensional space into two-dimensional plane coordinate points in the image plane CS through a perspective model. Therefore, converting the Q point in the camera CS to the Q' point in the image plane CS, the relevant expression obtained on the ground of the theorem of triangles is shown in equation (2).

$$[x y]^{T} = \frac{e}{Z_{b}} [X_{b} Y_{b}], Z_{b} [x y 1]$$

$$= \begin{bmatrix} e & 0 & 0 & 0 \\ 0 & e & 0 & 0 \\ 0 & 0 & 1 & 0 \end{bmatrix} [X_{b} Y_{b} Z_{b} 1]$$
 (2)

In equation (2), the second equation is the homogeneous matrix form of the first equation. *e* serves as the camera focal length. On the ground of this, calibrating the actual focal length of the camera can determine the conversion relation in the camera CS and the image plane CS. In the image CS shown in Figure 1, the relationship between the planar CS and the image CS is expressed in homogeneous matrix form, as shown in equation (3).

$$\begin{cases}
\left[\mu_{k} \ v_{j}\right]^{T} = \left[\frac{x}{c_{x}} + \mu_{0} \ \frac{y}{c_{y}} + v_{0}\right] \\
\left[\mu_{k} \ v_{j} \ 1\right]^{T} = \left[\begin{array}{cc} 1/c_{x} & 0 & \mu_{0} \\
0 & 1/c_{y} & v_{0} \\
0 & 0 & 1
\end{array}\right] \left[x \ y \ 1\right]
\end{cases} (3)$$

In equation (3), μ_k and ν_j represent the pixels in the k-th row and j-th column of the image CS. μ_0 and ν_0 represent the main points of the digital image. c_x and c_y represent

the actual distance per unit pixel in the μ and ν directions. The formula for converting the world CS obtained through combining equations (2) and (3) to the image CS is illustrated in equation (4).

$$Z_{b} \left[\mu_{k} \ v_{j} \ 1 \right] = \begin{bmatrix} 1/c_{x} & 0 & \mu_{0} \\ 0 & 1/c_{y} & v_{0} \\ 0 & 0 & 1 \end{bmatrix} \begin{bmatrix} e \ 0 \ 0 \ 0 \\ 0 \ e \ 0 \ 0 \\ 0 \ 0 \ 1 \ 0 \end{bmatrix}$$

$$= \begin{bmatrix} \Re L \\ 0 \ 1 \end{bmatrix} \left[X_{\varpi} \ Y_{\varpi} \ Z_{\varpi} \ 1 \right]$$

$$= \begin{bmatrix} e_{x} \ 0 \ \mu_{0} \ 0 \\ 0 \ e_{y} \ v_{0} \ 0 \\ 0 \ 0 \ 1 \ 0 \end{bmatrix} \begin{bmatrix} \Re L \\ 0 \ 1 \end{bmatrix} \left[X_{\varpi} \ Y_{\varpi} \ Z_{\varpi} \ 1 \right]$$

$$= W_{1} W_{2} Q_{\varpi} = W Q_{\varpi}$$

$$(4)$$

In equation (4), W_1 serves as the camera intrinsic matrix. W_2 serves as the camera extrinsic matrix. $Q_{\overline{w}}$ serves as the coordinates of objects in the real world. W represents the camera projection matrix. In real life, due to factors such as materials and processing, camera lenses exhibit different magnifications on the focal plane, leading to image distortion and geometric distortion. This reduces the accuracy of position detection. Lens distortion can be divided into two categories: radial distortion and tangential distortion. On the ground of camera calibration, it began to use Mask R-CNN for defect classification. This network structure is on the ground of Faster Region Convolutional Neural Network (Faster R-CNN) and incorporates a branch for semantic segmentation. It can achieve good instance segmentation on multiple samples without limiting image size. This network takes standardized high-resolution industrial workpiece images as input, with image sizes standardized to 224×224 pixels. The output of the network is the instance segmentation of surface defects on the workpiece, which includes the category and location of defects (determined by the Bounding Box coordinates), as well as the mask for each defect instance. The network utilizes Residual Network 101 (Resnet101) as its backbone network, which consists of 101 layers, including multiple convolutional layers, batch normalization layers, and ReLU activation functions. The Feature Pyramid Network (FPN) further refines the feature map, generating 5 feature layers with different resolutions and number of feature channels. In terms of special structure, the network integrates Mask R-CNN, which includes Region Proposal Network (RPN) for generating candidate regions, Region of Interest (ROI) align layer for aligning candidate regions with feature maps, and outputting the final classification and segmentation results through a fully connected layer. The schematic diagram of the Mask R-CNN architecture is showcased in Figure 3.

Figure 3 shows that the Mask R-CNN architecture constructed in the study mainly uses Resnet101 and FPN as the skeleton of the actual network to extract relevant image features and obtain corresponding feature maps. On this basis, the RPN uses a 3 * 3 convolution method to reduce the dimensionality of the feature map, and uses a 1 * 1 convolution



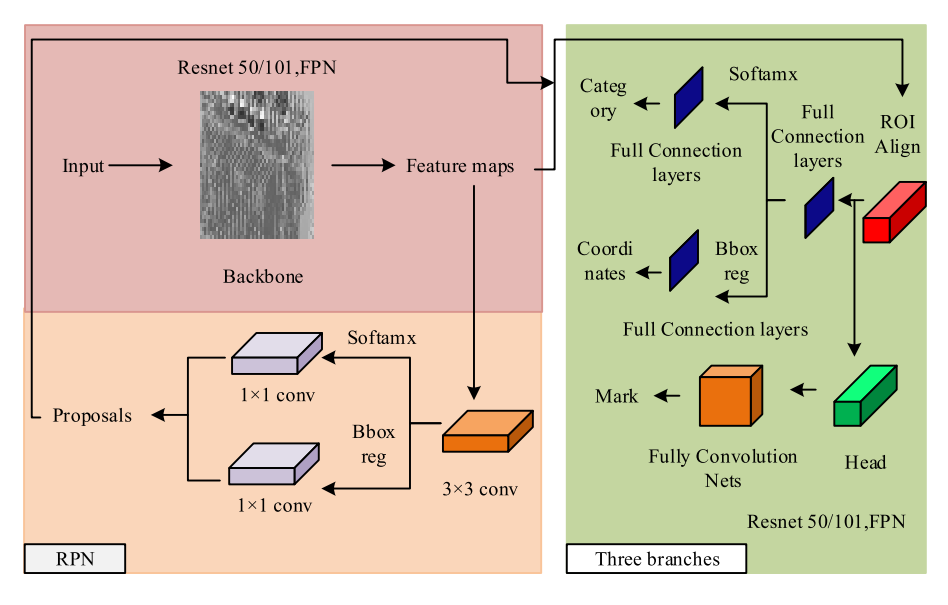


FIGURE 3. Schematic diagram of the overall architecture of Mask R-CNN.

as two paths. A path is used to binarize candidate frames to determine their foreground and background. The other group performs regression operations to find the coordinates of candidate boxes. Finally, Mask R-CNN proposed an ROI distribution model to replace the quantization operation of ROI points in Faster R-CNN. Then it uses bilinear interpolation to elevate the candidate frame coordinates to floating-point positions, thereby achieving matching in the original image and the feature image. The final candidate area is further divided into three branches to perform N-classification, further localization, and Mask instance segmentation on the candidate objects. The Mask R-CNN algorithm was chosen due to its high efficiency and accuracy in object detection and instance segmentation. This algorithm can accurately identify and segment individual instances in the image, which is crucial for automatically planning the polishing path of workpieces with complex defects. It provides powerful feature representation capabilities through deep learning, generalizes various defects, and predicts framework coordinates for precise localization. The integration of Mask R-CNN and robot systems enables automated polishing without the need for manual teaching, and improves polishing efficiency and quality through intelligent decision-making based on historical data.

In addition to conventional accuracy, the evaluation indicators for Mask R-CNN networks in the experiment also need to consider the Intersection over Union (IoU), which is the core evaluation indicator for object detection and instance segmentation networks. The relevant expressions are shown in equation (5).

$$\hbar = \frac{NI \cap G}{NI \cup G} \tag{5}$$

In equation (5), \hbar represents the intersection union ratio. NI represents the predicted result. G represents the true label.

B. ROBOT SENSOR SIGNAL PROCESSING AND POLISHING CONTROL TECHNOLOGY

On the basis of optimizing the visual inspection system of industrial robots, corresponding polishing experiments can be carried out. However, to achieve good contact force control during the actual polishing process, it is necessary to process the actual collected signals from the six-dimensional sensors accordingly. The process includes data filtering, gravity compensation, and data decoupling. Among them, a second-order digital Butterworth low-pass filter was designed to digitally filter the signal of a six-dimensional force sensor, and its related expression is shown in equation (6) [27].

$$|H_{a}(i\Omega)|^{2} = \frac{1}{1 + \left(\frac{\Omega}{\Omega_{c}}\right)^{2}}, H(z) = \frac{Y(z)}{X(z)}$$

$$= \frac{\sum_{\kappa=0}^{N} d_{\kappa} z^{-\kappa}}{1 + \sum_{\kappa=0}^{N} a_{\kappa} z^{-\kappa}}$$
(6)

In equation (6), $H_a(i\Omega)$ represents the low-pass mode squared function of the Butterworth filter. Ω represents the cut-off angular frequency of the filter. i represents the frequency coefficient. H(z) represents the transfer function of the Butterworth filter. N represents the order of the filter. Gravity compensation mainly considers the influence of the sensor's own gravity and the load's gravity on the measured force/torque. The actual values of the compensated force and torque in the experiment are expressed as equation (7) [28].

$$\begin{bmatrix} F' \ M' \end{bmatrix} = \begin{bmatrix} f_x' f_y' f_z' \ m_x' \ m_y' \ m_z' \end{bmatrix} = \begin{bmatrix} F - F_r \\ M - M_r \end{bmatrix}$$
(7)

In equation (7), F and F' represent the forces before and after compensation, and f is its internal element. M and M' represent the compensated front and rear pose moments, and m is its internal element. In data decoupling research,

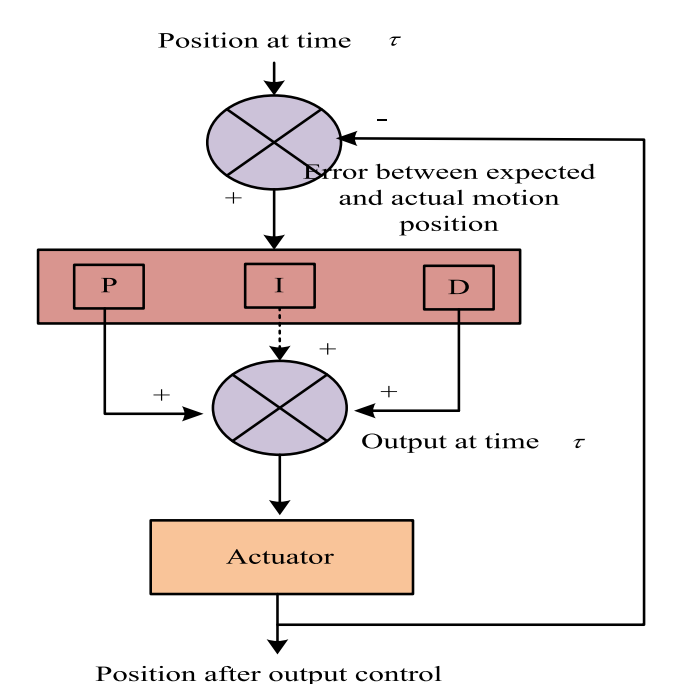


FIGURE 4. PID controller architecture diagram.

static decoupling algorithms on the ground of coupling error modeling are used to decouple six-dimensional sensor data [29].

After three steps, research began on the control strategy for the actual polishing effect of industrial robots. Traditional six-dimensional force sensors are also affected by inertial forces during high-speed motion. In research, when the robot does not come into contact with the workpiece, there is no need to control its force. During the demonstration period, the operator can press the button on the power feedback handle and inform the system whether to enter the polishing state on the ground of the input signal. Due to the slow teaching speed and the movement speed of the robotic arm during polishing, the influence of inertial force is ignored, thus simplifying the mathematical model of the control algorithm. In the teaching method, the operator uses a six-dimensional force sensor for controlling the force/torque. The end robot system records all teaching positions and force/torque information. In autonomous mode, the robot arm moves according to the teaching position, divided into non-polishing period and polishing period. During the non-polishing period, PID control is used according to the teaching position without applying any force. During the polishing period, position impedance is used to control the adhesive force/torque information, achieving autonomous force position control during the polishing period.

Due to the generally good repeatability of research on robotic arms for established movements, only slight motion control is required during the free following stage to ensure the trajectory of the robotic arm. Therefore, the study chose incremental PID control, whose architecture is shown in Figure 4 [30].

Figure 4 shows that the first step is to input the position at time τ , and then use a PID controller to control the expected position error at time τ , thereby outputting the control variable. After the operation of the actuator, its final output position is determined. Among them, the actual output expression of the controller at the τ -th sampling time is shown in equation (8).

$$\phi_{\tau} = B_P \left[\theta_{\tau} + \frac{T}{T_I} \sum_{j=0}^{\tau} \theta_j + T_D \frac{\theta_{\tau} - \theta_{\tau-1}}{T} \right]$$
(8)

In equation (8), ϕ_{τ} represents the actual output value at the τ -th sampling time. B_P represents the proportional coefficient. T is the sampling period. T_I and T_D represent integral and differential coefficients. θ_{τ} represents the error between the expected position and the actual position. The expected position is given by the teaching data, and the actual motion position can be calculated by feedback data from the robotic arm encoder. The output expression at the sampling time of $\tau - 1$ is shown in equation (9).

$$\phi_{\tau-1} = B_P \left[\theta_{\tau-1} + \frac{T}{T_I} \sum_{j=0}^{\tau-1} \theta_j + T_D \frac{\theta_{\tau-1} - \theta_{\tau-2}}{T} \right]$$
(9)

By combining and subtracting equations (8) and (9), the actual output control quantity of the PID control method can be obtained. Its expression is shown in equation (10).

$$\Delta \phi_{\tau} = \phi_{\tau} - \phi_{\tau - 1} = B_{P} \left[\phi_{\tau} - \phi_{\tau - 1} + \frac{T}{T_{I}} \phi_{\tau} + T_{D} \frac{\phi_{\tau} - 2\phi_{\tau - 1} + \phi_{\tau - 2}}{T} \right]$$

$$= B_{P} \left(1 + \frac{T}{T_{I}} + \frac{T_{D}}{T} \right) \phi_{\tau} - B_{P} \left(1 + \frac{2T_{D}}{T} \right) \phi_{\tau - 1} + B_{P} \frac{T_{D}}{T} \phi_{\tau - 2}$$
(10)

In addition, the position impedance used during the polishing period to control the adhesion force/torque information follows the expected position and expected force/torque during the polishing control. In the polishing control process, due to the lack of passive flexible components such as hydraulic cylinders and springs, it is necessary to actively and smoothly control them. IC is mainly divided into force feedback type and position type IC. The ideal IC model in force feedback IC can be regarded as a spring damping model. The mathematical modeling analysis of this model can be expressed using second-order differential equations, which have three forms of expression as shown in equation (11).

$$\begin{cases}
M_d \ddot{V} + U_d \dot{V} + \rightarrow_d (V - V_d) = -\ell \\
M_d \ddot{V} + U_d (\dot{V} - \dot{V}_d) + \rightarrow_d (V - V_d) = -\ell \\
M_d (\ddot{V} - \ddot{V}_d) + U_d (\dot{V} - \dot{V}_d) + \rightarrow_d (V - V_d) = -\ell
\end{cases}$$
(11)

In equation (11), M_d represents the expected inertia matrix. \ddot{V} and \dot{V} represent the actual speed and acceleration. U_d represents the expected damping matrix. \rightarrow_d represents the expected stiffness matrix. V and V_d represent actual motion



and expected motion positions. ℓ represents contact force. \dot{V}_d and \ddot{V}_d represent the expected speed and acceleration. When introducing force deviation into the impedance mathematical model and using the third impedance representation model, the actual expression of the model is shown in equation (12).

$$\mathbf{M}_d \left(\ddot{V} - \ddot{V}_d \right) + U_d \left(\dot{V} - \dot{V}_d \right) + \rightarrow_{d} (V - V_d) = \vartheta_{\pi} \quad (12)$$

In equation (12), ϑ_{π} represents the force deviation. The expected impedance equation obtained by changing equation (12) using Lagrange is expressed as equation (13).

$$\Lambda(s) = \frac{\vartheta(s)}{\vartheta_{\pi}(s)} = \frac{1}{M_d s^2 + U_d s + \lambda_d}$$
(13)

In equation (13), Λ (s) represents the expected impedance. s represents the domain, which is an extension of the frequency domain. The calculation difficulty of force feedback IC is relatively high, while position type IC does not have a force feedback loop, and there is no need to solve specific dynamic models, making the control relatively simple. Therefore, the study utilizes positional IC to control the following motion of robotic arm polishing. For positional IC, there is always fluctuation in the relevant data of the six-dimensional sensor during the actual teaching polishing process, so it is necessary to pre-process the teaching force data in advance. This study selected 100 teaching points as sliding windows and calculated the average teaching force. Then it removes irrelevant discrete points that deviate by 80% from the average value due to small protrusions on the processed surface or offline sampling, and uses neighborhood interpolation to interpolate the removed points. When the change in force/torque does not exceed 10%, the control system will not change the required force/torque value. This can maintain the force at a certain level as much as possible during the polishing process, avoiding system instability caused by frequent adjustment of posture, which can affect the actual polishing results. Among them, the positional IC architecture combined with the six-dimensional force sensor is showcased in Figure 5.

Figure 5 shows that the position-based IC architecture mainly consists of a combination of IC outer loop and PID position control inner loop. In the position-based IC method, the theoretical motion position of the robotic arm is calculated by subtracting the position deviation from the teaching position. Then, on the ground of this, it uses the inverse kinematics of the robotic arm for getting the actual relevant rotation angles of each joint, which is essentially the control pulse. The control pulse is transmitted to the relevant position control loop and PID control is applied to the position of the industrial robot arm, so that the arm can reach the given target position. At this point, one cycle of position IC can be completed. When constructing a position-based IC method, the impedance model needs to be discretized first. This study utilizes bilinear transformation to transform the s domain in equation (13) into the z' domain, and the transformed expression is shown in equation (14).

$$\begin{cases} \Lambda\left(z'\right) = \frac{\vartheta\left(z'\right)}{\vartheta_{\pi}\left(z'\right)} = \frac{\mathrm{T}^{2}\left(z'+1\right)^{2}}{\alpha_{1}z'^{2} + \alpha_{2}z' + \alpha_{3}} \\ \alpha_{1} = 4\mathrm{M}_{d} + 2U_{d}\mathrm{T} + \lambda_{d}\mathrm{T}^{2}, \alpha_{2} = -8\mathrm{M}_{d} + 2\lambda_{d}\mathrm{T}^{2}, \\ \alpha_{3} = 4\mathrm{M}_{d} - 2U_{d}\mathrm{T} + \lambda_{d}\mathrm{T}^{2} \end{cases}$$

$$(14)$$

In equation (14), z' represents the extension of the s domain, i.e. the delay operation in the s domain. α_1 , α_2 , and α_3 represent angular frequencies. The differential expression of the IC obtained from this is shown in equation (15).

$$\vartheta\left(n'\right) = \frac{\mathsf{T}^2}{\alpha_1} \left(\vartheta_\pi\left(n'\right) + 2\vartheta_\pi\left(n'-1\right) + \vartheta_\pi\left(n'-2\right)\right) \\ -\frac{\alpha_2}{\alpha_1}\vartheta\left(n'-1\right) - \frac{\alpha_3}{\alpha_1}\vartheta\left(n'-2\right) \tag{15}$$

In equation (15), ϑ (n') represents the differential expression of the IC. Due to the fact that M_d , U_d , and $\rightarrow d$

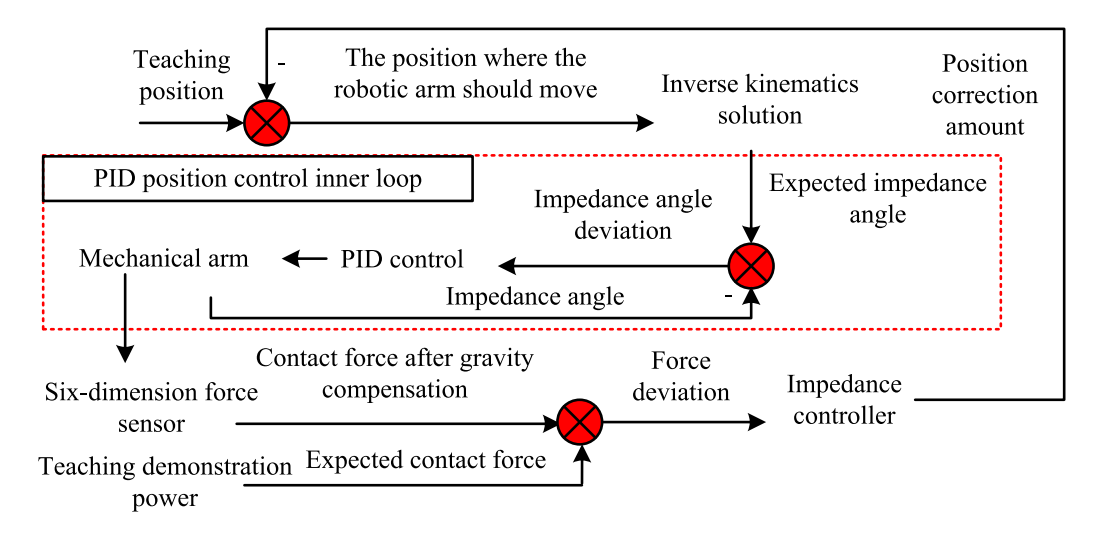


FIGURE 5. Schematic diagram of positional IC architecture combined with six-dimensional force sensors.



are all semi positive definite diagonal matrices, the IC method actually provided can control various methods in three-dimensional space accordingly. In response to the demand for improving the intelligence of the system, the research aims to automatically plan the path for workpieces with defects but good substance in the end robotic arm system on the ground of the results of Mask R-CNN visual inspection, and complete autonomous polishing without the need for teaching. Therefore, for defects such as scratches, stains, and rust on the surface of the processed workpiece, the study first locates the external rectangle of the Mask, which is the predicted frame coordinate, on the ground of the defect recognition results. Next, it slowly lowers the robot arm at a speed of 1mm/s, gently lifts it when there is a sudden change in contact force in the z-domain, and considers it as the defect location. Finally, the Mask R-CNN algorithm is used to extract the polishing force data of similar materials with the same defect, and it is used as the required force energy for polishing. Regarding the defects such as burrs, defects, and residual glue that appear at the edges during the processing, this study first determines the location of the defects, and then obtains the boundaries and rotation angles of the defects through a measurement system. Then it approaches the defect point 45 degrees from the tangent direction of the robot arm, and finally achieves force controlled polishing on the ground of the data in the database.

IV. VISUAL CONTROL AND POLISHING EXPERIMENTAL VERIFICATION

To verify the effectiveness of the robot polishing system designed in this study, which utilizes machine vision control algorithms and six-dimensional force sensors, the visual system validation and overall polishing system validation were conducted in this section.

A. VERIFICATION OF SURFACE DEFECT DETECTION ON WORKPIECES

In visual system validation, it is necessary to configure and train the Mask R-CNN. Research utilized PyTorch1 as a deep learning architecture to build a substantial network, with the COCO dataset pre-training the main backbone network. This database was provided by industrial partners and was widely collected from the surface of workpieces in actual production environments, containing images of various material types and different defect categories. During the database construction process, images were pre-processed by a professional team, including denoising, contrast enhancement, and size standardization, to ensure data quality. The data annotation work was the responsibility of domain experts, who use annotation software to classify and locate each defect instance in the image, and accurately annotate pixel level masks. The entire database contained over 10000 images, covering 5 main materials and at least 15 types of defects. To verify the generalization of the model and evaluate its accuracy, the database was reasonably divided into a training set (accounting for 70%), a validation set (accounting for 15%), and a testing set (accounting for 15%). In the experimental environment, Intel (R) Core (TM) i5-7500 was selected as the processor, Windows 7 was selected as the system, 16GB of memory was selected, and 8GB of memory was used for the graphics card. The results of the loss changes during the training process of Mask R-CNN network are showcased in Figure 6.

Figure 6 (a) shows that the classification loss of the RPN network in Mask R-CNN converged around 20000 iterations, and the predicted regression loss showed a fluctuating decrease. Figure 6 (b) shows that both the classification loss curve and the prediction box regression loss curve showed a decreasing trend in volatility, but neither showed a zero value. Figure 6 (c) shows that the overall loss curve of the Mask R-CNN network was basically consistent with the trend of the predicted box regression loss curve. On the ground of the training results, the performance and size detection of the Mask R-CNN were analyzed, and the indicators selected were mean IOU (mIOU), Average Precision (AP), and Mean Average Precision (mPA). The outcomes are showcased in Table 1.

In Table 1, L1~L3 represent the length of wood in linear detection. R1 and R2 are the radii of circles in arc detection. Table 1 shows that the network mAP value proposed in the study reached 91.54%, with an average detection time of 3fps. This indicates that it can satisfy the requirements of defect detection in small workpiece polishing operations, and the segmentation accuracy meets the requirements of use. The error between the measured value and the true value in straight line detection did not exceed 1mm, with a maximum error of 0.36mm. The maximum measurement error between the measured value and the true value in arc detection was 1.02mm, with an average error of 0.33mm, which meets the actual measurement requirements.

According to Table 2, in comparative evaluations, Mask R-CNN achieved an accuracy of 91.54%, surpassing Faster R-CNN by 2.45% and YOLOv4 by 3.27%. It also exceeded Faster R-CNN by 3.10% and YOLOv4 by 5.00% in Recall, with a corresponding F1 score of 90.87. Training time for Mask R-CNN was 4 hours, which was 33.33% shorter than Faster R-CNN's 6 hours and 20% less than YOLOv4's 5 hours. Mask R-CNN's testing time was 30 minutes, 33.33% faster than Faster R-CNN and 16.67% faster than YOLOv4. It contained 40 million parameters, 33.33% fewer than Faster R-CNN's 60 million and 20% less than YOLOv4's 50 million. Additionally, Mask R-CNN operated with moderate hardware requirements, unlike the high requirements of Faster R-CNN and YOLOv4.

To further validate the superiority of Mask R-CNN, this study introduced the use of Improved Particle Swarm Optimization (IPSO), Adaptive Control (AC), and Binocular Vision Algorithm (BVA) to compare polishing errors under visual detection. The experimental materials selected included rusted alloy, alienated alloy, and copper plated thin plate, and the outcomes are showcased in Table 3.



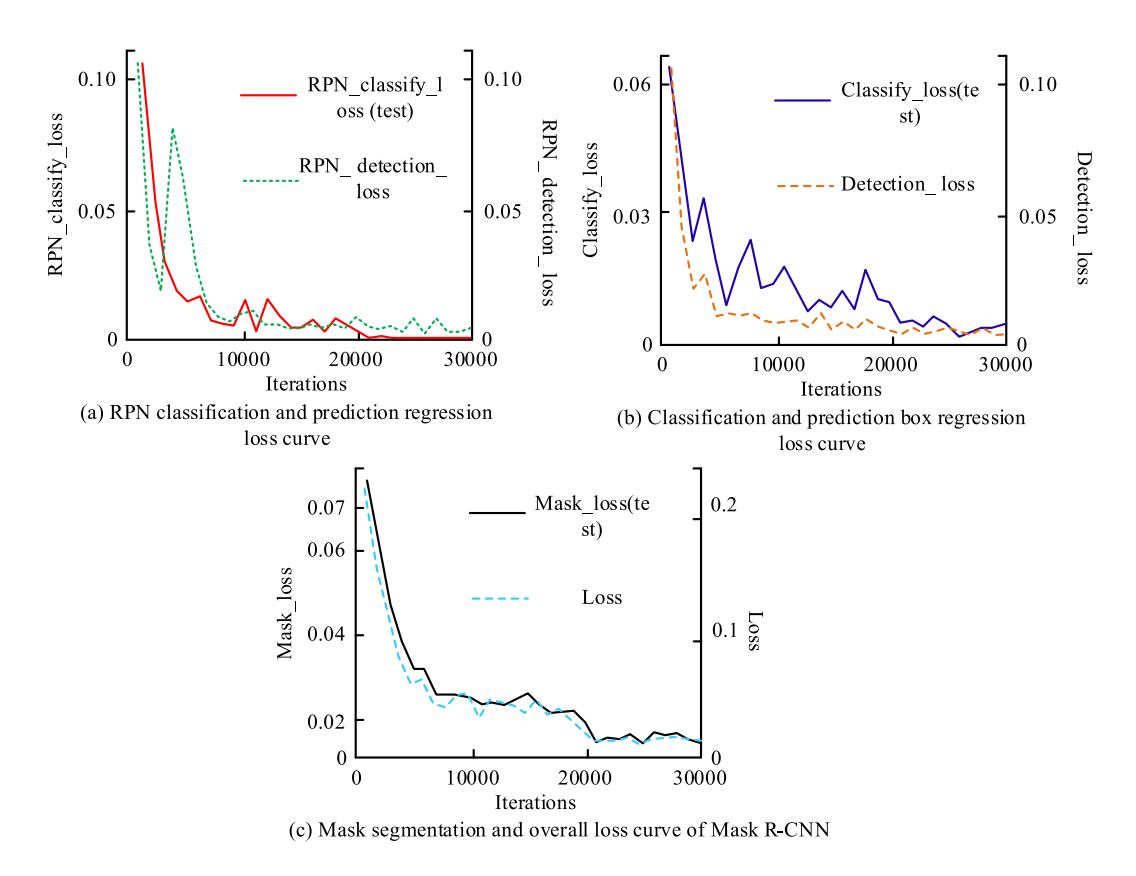


FIGURE 6. Results of loss changes during Mask R-CNN network training.

TABLE 1. Performance and size detection results of mask R-CNN network.

		Performance	e Analysis of Mas	k R-CNN Network			
- AP mAP mIoU Training time Mean							
Resnet101+FPN	92.74%	91.54%		90.91%	40.59h	3.00fps	
Resnet50+FPN	86.66%	85.619	½	84.46%	28.49h	5.00fps	
	C	Comparison betwee	n measured and tr	rue values in size de	tection		
-	L1	L2	L3	L4	R1	R2	
Measurement value	80.22mm	80.14mm	50.32mm	50.58mm	49.28mm	59.34mm	
True value	80.55mm	80.44mm	50.15mm	50.22mm	50.30mm	59.95mm	

Table 3 shows that the polishing errors under the visual detection guidance of the proposed network were 8.9mm, 8.5mm, and 8.3mm in width, and 1.0mm, 1.2mm, and 1.5mm in depth, respectively, among the three materials, which are lower than the comparison algorithms. Overall, Mask R-CNN is effective in visual inspection of polishing and can effectively avoid abnormal damage during polishing.

B. SIGNAL PROCESSING ANALYSIS OF SIX-DIMENSIONAL FORCE SENSOR

On the basis of visual detection verification, this study began to process the signals collected by six-dimensional sensors. Due to the more intuitive visualization effect of data filtering, data filtering was analyzed separately in the research experiment. During the actual polishing process, the force/torque waveform changes obtained by starting the electric grinding without load are shown in Figure 7.

Figure 7 (a) shows that under no load, the range of force variation on the z-axis after the start of the electric mill was larger than that on the x-axis and y-axis, ranging from -1.0N to 1.5N, and the other two axes were both between -0.5N and 1.0N. Figure 7 (b) shows that the range of three-axis torque variation was between -0.005 and $0.005N \bullet cm$, with the y-axis having the lowest range of variation. Overall, due to



Metric/Algorithm	Mask R-CNN	Faster R-CNN	YOLOv4	Improvement over Faster R-CNN (%)	Improvement over YOLOv4 (%)
Accuracy (%)	91.54	89.30	88.65	+2.45	+3.27
Recall (%)	90.20	87.50	85.80	+3.10	+5.00
F1 score	90.87	88.40	87.10	+2.79	+4.25
Training time (h)	4	6	5	-33.33	-20.00
Testing time (min)	30	45	35	-33.33	-16.67
Parameter count	40	60	50	-33.33	-20.00

High

High

TABLE 2. Comparative performance metrics of mask R-CNN with faster R-CNN and YOLOv4.

Moderate

TABLE 3. Comparison of polishing errors under visual inspection.

(M) Hardware

requirement

-	BVA		AC		IPSO		Mask R-CNN	
-	Width error	Depth error						
Rusted alloy	10.9mm	9.6mm	10.1mm	8.5mm	12.1mm	5.1mm	8.9mm	1.0mm
Alienated alloy	11.2mm	8.4mm	12.4mm	8.5mm	13.0mm	4.8mm	8.5mm	1.2mm
Copper plated thin plate	13.2mm	7.5mm	11.1mm	10.2%	11.5mm	3.5mm	8.3mm	1.5mm

the significant fluctuations in the vibration influence/torque data of the electric mill itself, the peak force could reach 1.8N. Therefore, numerical filtering operation was required. Before verifying the effectiveness of the research method, the actual vibration signal was first subjected to Fourier transform operation to analyze the frequency spectrum of noise. The results are shown in Figure 8.

Figure 8 shows the force/torque vibration spectrum of the six-dimensional force sensor during no-load starting of the electric mill through Fourier transform. In Figure 8 (a), the vibration spectrum of the X-axis showed a significant peak at a specific frequency, with an amplitude of approximately 0.045, while the Y-axis and Z-axis had three and two significant fluctuation regions, respectively. This may be related to the physical characteristics and operational vibration modes of the electric mill. Figure 8 (b) shows that the main energy of the three axes in the torque vibration spectrum was concentrated in the frequency range of 200Hz to 300Hz, indicating the resonance frequency of the equipment. These pieces of information are crucial for understanding the dynamic behavior of the system during the polishing process and guiding subsequent signal processing strategies, such as using low-pass filters to reduce high-frequency noise and improve measurement accuracy. Therefore, the research method was used to perform digital filtering on it. The six-dimensional sensor signal changes after low-pass filter processing are shown in Figure 9.

Figure 9 shows the time-domain curve changes of the six-dimensional force sensor signal after being processed by a low-pass filter. In Figure 9 (a), the three-axis time-domain curve of the force showed a significant reduction in fluctuations after data filtering, maintaining a stable range within 0.1N, indicating that the filtering process effectively reduced high-frequency noise in the signal. Figure 9 (b) depicts the three-axis time-domain curve of the torque signal, which also showed a more stable change after filtering, with fluctuations controlled within 0.001N·cm. This indicates that the filtering method has successfully removed high-frequency fluctuations in the torque signal, providing high-quality data for precise force control in experiments.

C. ANALYSIS OF POLISHING EXPERIMENT RESULTS

On the basis of visual inspection and data processing results, research was conducted to verify the designed automatic polishing system through practical experiments. Firstly, a comparison was made between the results of system demonstration polishing and autonomous polishing. Four materials were selected in the experiment, namely web plate material corresponding to 1, weld material corresponding to 2, pipe material corresponding to 3, and wood corresponding to 4. The comparison results are shown in Table 3. The comparison outcomes are showcased in Table 4.

In Table 4, A to C represent the X, Y, and Z axis directions. D to F represents the force in the x, y, and z-axis directions.



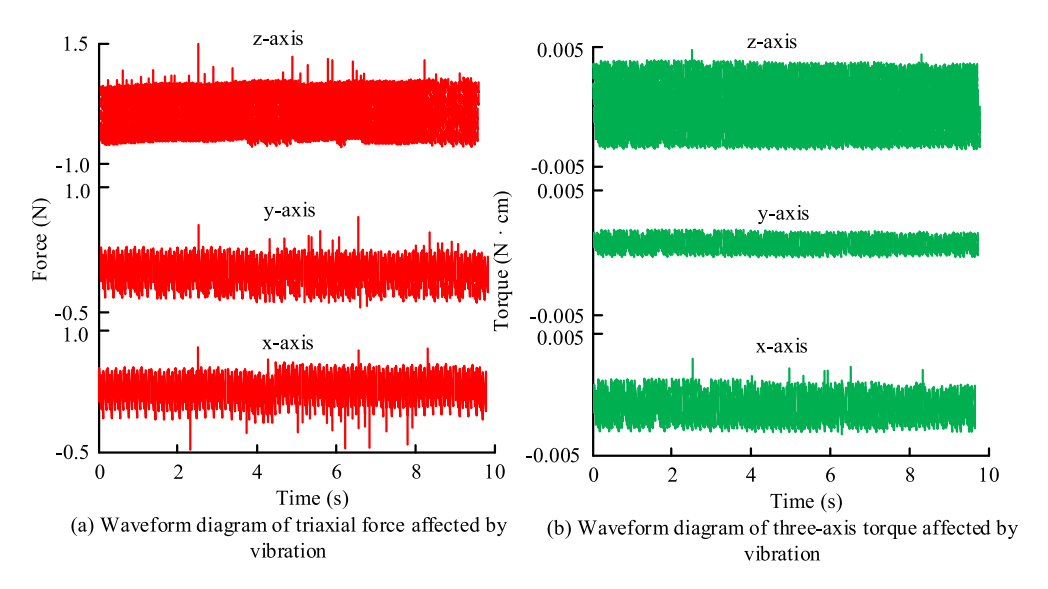


FIGURE 7. Waveform diagram of force/torque in the three-axis direction affected by vibration.

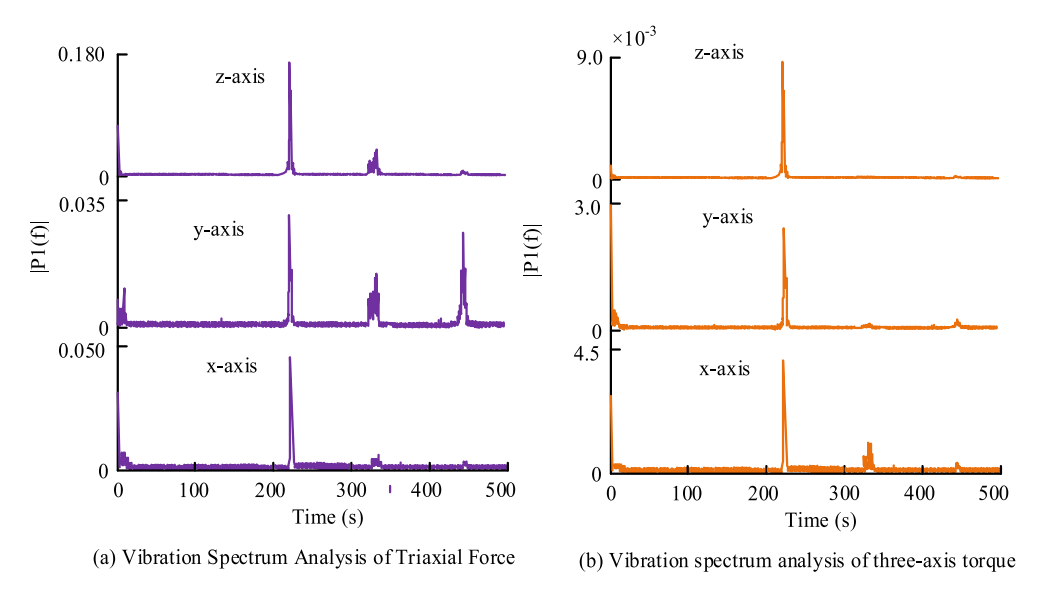


FIGURE 8. Spectral analysis results of force/torque vibration in the three-axis direction.

G to I represents the torque in the x, y, and z-axis directions. Z represents the maximum error, and P represents the average error. Table 2 showed that the control methods used in the automatic polishing system could effectively follow the teaching results in the polishing of all four materials. The actual level following error was less than 1mm, and it could quickly respond to changes in polishing contact force and adjust the posture. Overall, the industrial robots studied and designed had good results in polishing, which can meet the polishing needs of small workpieces. To further verify the effectiveness of the constant force control of the position controller used in the study, the contact force data with and without constant force control were compared, and the results are shown in Figure 10.

Figure 10 shows the experimental results of applying a position type constant force controller to control the output force of industrial robots during the polishing. This figure verified the effectiveness of the constant force controller by comparing the contact force data under two conditions: constant force control and no constant force control. The force control curves from different perspectives are shown in sections (a) and (b) of the figure. In the case of constant force control, the controller could dynamically adjust the output force of the robot based on the preset force target value, so as to maintain the contact force within a stable range. This control method could effectively avoid workpiece damage caused by excessive force, while also ensuring the uniformity and consistency of the polishing process. Through constant force

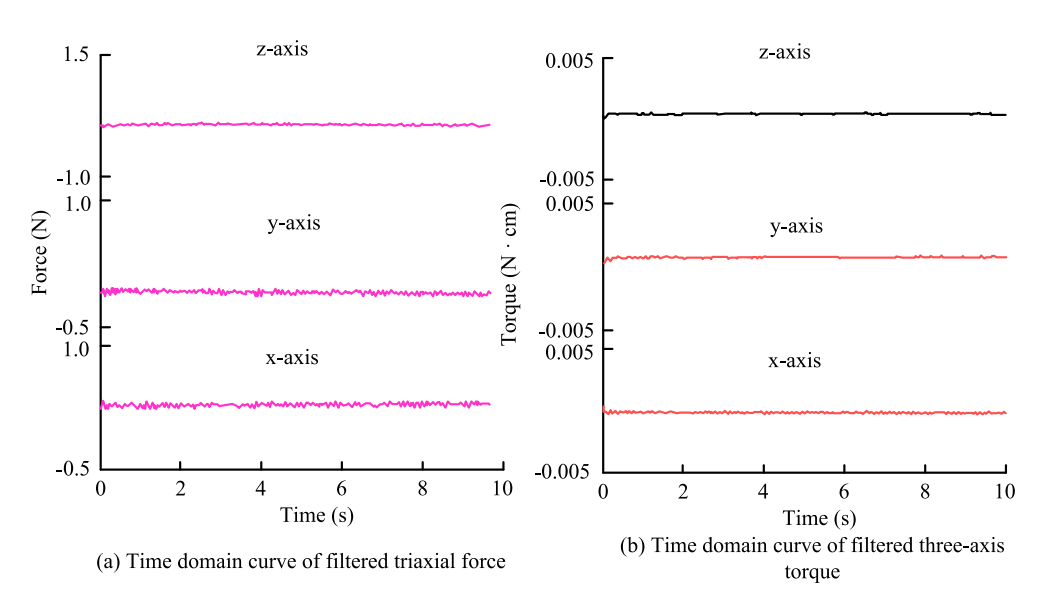


FIGURE 9. The change results of the six-dimensional sensor signal after low-pass filter filtering.

TABLE 4. Comparison between teaching position/force and following position/force.

P(1) 0.21mm 0.34mm 0.55mm 0.07N 0.31N 0.68N 0.03N·cm 0.03N·cm 0.03N·cm Z(2) 2.25mm 2.03mm 3.93mm 0.56N 2.56N 4.91N 0.16N·cm 0.12N·cm 0.14N·cm P(2) 0.05mm 0.17mm 0.44mm 0.11N 0.33N 0.45N 0.03N·cm 0.03N·cm 0.04N·cm Z(3) 0.94mm 0.96mm 4.04mm 0.21N 4.11N 2.93N 0.05N·cm 0.02N·cm 0.04N·cm P(3) 0.28mm 0.40mm 0.83mm 0.02N 0.40N 0.31N 0.01N·cm 0.01N·cm 0.01N·cm Z(4) 1.55mm 1.47mm 4.56mm 0.90N 2.66N 2.71N 0.29N·cm 0.13N·cm 0.09N·cm										
P(1) 0.21mm 0.34mm 0.55mm 0.07N 0.31N 0.68N 0.03N·cm 0.03N·cm 0.03N·cm Z(2) 2.25mm 2.03mm 3.93mm 0.56N 2.56N 4.91N 0.16N·cm 0.12N·cm 0.14N·cm P(2) 0.05mm 0.17mm 0.44mm 0.11N 0.33N 0.45N 0.03N·cm 0.03N·cm 0.04N·cm Z(3) 0.94mm 0.96mm 4.04mm 0.21N 4.11N 2.93N 0.05N·cm 0.02N·cm 0.04N·cm P(3) 0.28mm 0.40mm 0.83mm 0.02N 0.40N 0.31N 0.01N·cm 0.01N·cm 0.01N·cm Z(4) 1.55mm 1.47mm 4.56mm 0.90N 2.66N 2.71N 0.29N·cm 0.13N·cm 0.09N·cm	-	A	В	С	D	Е	F	G	Н	I
Z(2) 2.25mm 2.03mm 3.93mm 0.56N 2.56N 4.91N 0.16N·cm 0.12N·cm 0.14N·cm P(2) 0.05mm 0.17mm 0.44mm 0.11N 0.33N 0.45N 0.03N·cm 0.03N·cm 0.04N·cm Z(3) 0.94mm 0.96mm 4.04mm 0.21N 4.11N 2.93N 0.05N·cm 0.02N·cm 0.04N·cm P(3) 0.28mm 0.40mm 0.83mm 0.02N 0.40N 0.31N 0.01N·cm 0.01N·cm 0.01N·cm Z(4) 1.55mm 1.47mm 4.56mm 0.90N 2.66N 2.71N 0.29N·cm 0.13N·cm 0.09N·cm	Z(1)	2.53mm	2.34mm	4.80mm	0.72N	3.11N	6.03N	0.53N·cm	0.13N·cm	0.20N·cm
P(2) 0.05mm 0.17mm 0.44mm 0.11N 0.33N 0.45N 0.03N·cm 0.03N·cm 0.04N·cm Z(3) 0.94mm 0.96mm 4.04mm 0.21N 4.11N 2.93N 0.05N·cm 0.02N·cm 0.04N·cm P(3) 0.28mm 0.40mm 0.83mm 0.02N 0.40N 0.31N 0.01N·cm 0.01N·cm 0.01N·cm 0.01N·cm Z(4) 1.55mm 1.47mm 4.56mm 0.90N 2.66N 2.71N 0.29N·cm 0.13N·cm 0.09N·cm	P(1)	0.21mm	0.34mm	0.55mm	0.07N	0.31N	0.68N	0.03N·cm	0.03N·cm	0.03N·cm
Z(3) 0.94mm 0.96mm 4.04mm 0.21N 4.11N 2.93N 0.05N·cm 0.02N·cm 0.04N·cm P(3) 0.28mm 0.40mm 0.83mm 0.02N 0.40N 0.31N 0.01N·cm 0.01N·cm 0.01N·cm Z(4) 1.55mm 1.47mm 4.56mm 0.90N 2.66N 2.71N 0.29N·cm 0.13N·cm 0.09N·cm	Z(2)	2.25mm	2.03mm	3.93mm	0.56N	2.56N	4.91N	0.16N·cm	0.12N·cm	0.14N·cm
P(3) 0.28mm 0.40mm 0.83mm 0.02N 0.40N 0.31N 0.01N·cm 0.01	P(2)	0.05mm	0.17mm	0.44mm	0.11N	0.33N	0.45N	0.03N·cm	0.03N·cm	0.04N·cm
Z(4) 1.55mm 1.47mm 4.56mm 0.90N 2.66N 2.71N 0.29N·cm 0.13N·cm 0.09N·c	Z(3)	0.94mm	0.96mm	4.04mm	0.21N	4.11N	2.93N	0.05N·cm	0.02N·cm	0.04N·cm
	P(3)	0.28mm	0.40mm	0.83mm	0.02N	0.40N	0.31N	0.01N·cm	0.01N·cm	0.01N·cm
P(4) 0.23mm 0.34mm 0.60mm 0.18N 0.22N 0.49N 0.02N·cm 0.05N·cm 0.02N·c	Z(4)	1.55mm	1.47mm	4.56mm	0.90N	2.66N	2.71N	0.29N·cm	0.13N·cm	0.09N·cm
	P(4)	0.23mm	0.34mm	0.60mm	0.18N	0.22N	0.49N	0.02N·cm	0.05N·cm	0.02N·cm

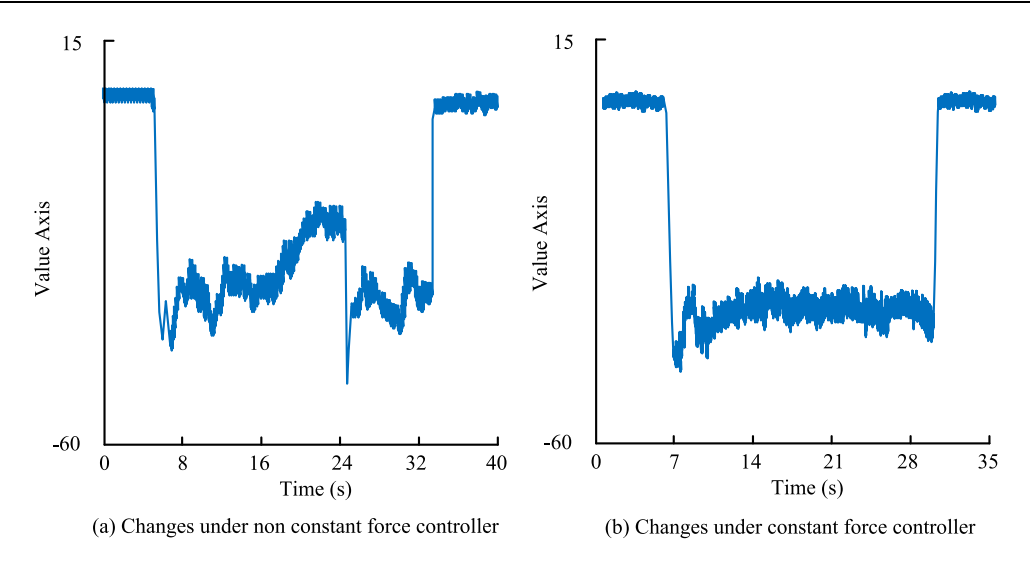


FIGURE 10. Contact force data results with/without constant force control.

control, the robot could process the surface of the workpiece more finely during the polishing, improving the polishing quality. In contrast, in the non-constant force control, the output force of the robot fluctuated greatly, making it difficult



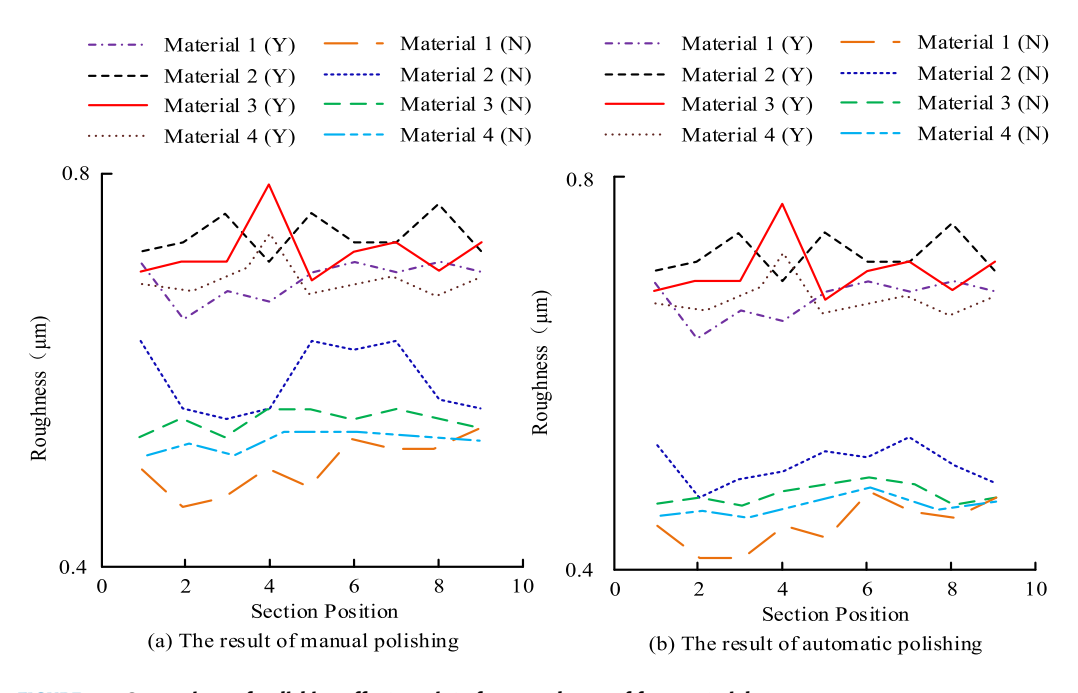


FIGURE 11. Comparison of polishing effects on interface roughness of four materials.

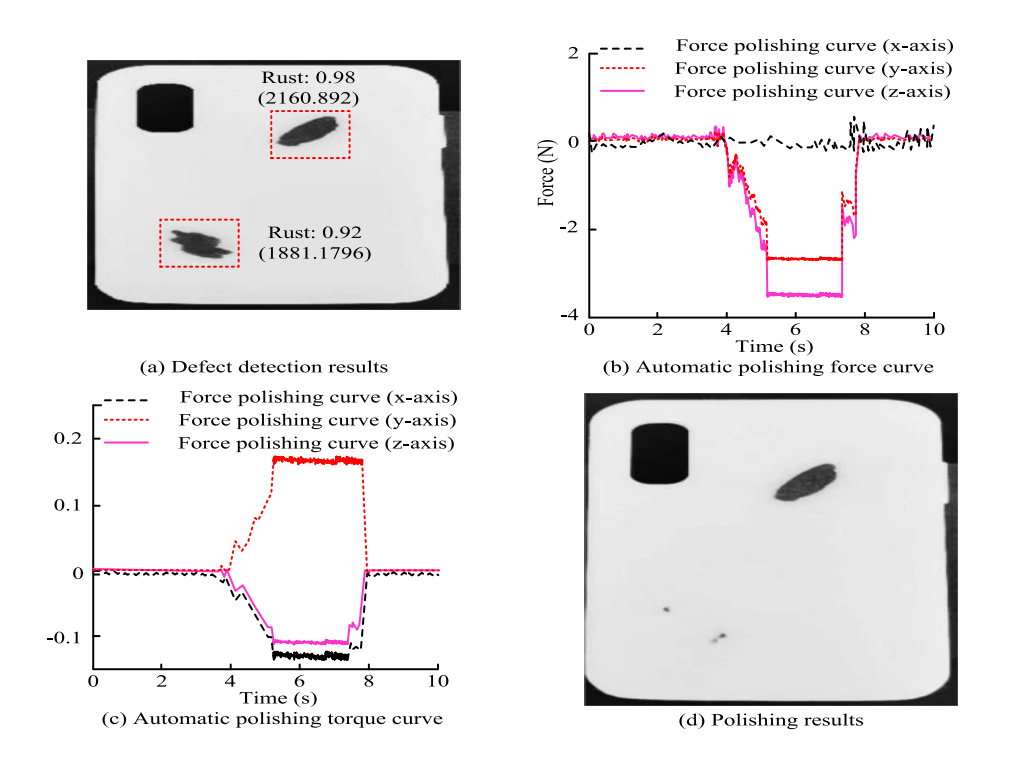


FIGURE 12. Actual automatic polishing effect.

to maintain within an ideal range. This instability may lead to inconsistent polishing quality and even cause unnecessary damage to the workpiece. To verify the effectiveness of the designed industrial robot, a study was conducted to compare its interface roughness with four materials artificially polished. Nine points were selected for two measurements in the

experiment, and the average value was taken. The result is shown in Figure 11.

In Figure 11, Y represents before polishing and N represents after polishing. Figure 11 (a) shows that the stable roughness values of manual polishing on materials 1 and 2 were $0.475\mu m$ and $0.561\mu m$, while the roughness values



FIGURE 13. Comparison of four types of workpieces before and after polishing.

on Material 3 were $0.522\mu m$ and $0.515\mu m$, respectively. The system designed for research was applied to industrial robots for automatic polishing, and the stable roughness values on Materials 1 and 2 were $0.321\mu m$ and $0.489\mu m$, while the roughness values on Materials 3 and 4 were $0.491\mu m$ and $0.487\mu m$. Overall, the research-designed automatic polishing industrial robot has effectiveness and practicality, effectively reducing the roughness of the material surface. On this basis, to further verify the substantial polishing effect of the designed industrial robot, the study would be applied to the actual polishing of mobile phone cases, and the results are shown in Figure 12.

Figures 12 (a) and 12 (d) show that the autonomous polishing has completed most of the polishing of the defect location,

but there are still a few residues. Multiple polishing could complete the autonomous polishing of simple workpieces. The overall design of industrial robots had a good polishing effect and strong practicality. Figures 12 (b) and 12 (c) show that the variation trend of the y-axis and z-axis of the automatic polishing force curve was the same, while the x-axis showed a relatively stable fluctuation. The variation trend of the automatic polishing torque curve on the x-axis and z-axis was the same, but completely opposite to the y-axis.

As shown in Figure 13, the workpiece was generally polished accurately, which reflects the effectiveness of the control algorithm proposed in the study. Through visual inspection, the system could obtain the morphological information of the workpiece surface in real time, thereby planning the grinding path more accurately. The use of historical polishing data provides experience for the system, allowing it to make more intelligent decisions based on past polishing experience.

V. CONCLUSION

In response to the lack of contact force control and poor polishing effect in traditional industrial robots during actual polishing operations, a new autonomous polishing system for industrial robots was proposed in this study using visual control algorithms and six-dimensional force sensors, and its effectiveness was verified. Experimental results proved that the system performed well in visual defect detection. The mAP value of the Mask R-CNN reached 91.54%, and the average detection time was 3fps, which met the detection needs in small workpiece grinding operations. The improvement of the six-dimensional force sensor signal processing significantly improved the accuracy and stability of force control, and the three-axis time domain curve fluctuation of the torque was controlled within 0.001N·cm. Actual polishing experiments showed that the system had excellent performance in following performance and contact force control, with an average following error of less than 1mm, and could respond quickly to changes in polishing contact force. Compared with manual polishing, the surface roughness of the material after automatic grinding was significantly reduced, proving the effectiveness and practicability of the system. In addition, mobile phone case polishing experiments further demonstrated the potential of the system in practical industrial applications. Despite the use of visual control algorithms and six-dimensional force sensors, the adaptability and robustness of the algorithms may need to be further improved to cope with a wider range of environmental and workpiece surface conditions. Secondly, the depth of data processing and analysis needs to be strengthened, especially in improving the resistance of signal processing algorithms to noise. Future research needs to deepen algorithm optimization, integrate multi-modal sensing technology, explore the application of AR/VR in user interaction, integrate innovative solutions across disciplines, and evaluate the performance stability of the system in changing environments.



REFERENCES

- [1] J. Zhang, J. Liu, and S. Yang, "Trajectory planning of robot-assisted abrasive cloth wheel polishing blade based on flexible contact," *Int. J. Adv. Manuf. Technol.*, vol. 119, nos. 11–12, pp. 8211–8225, Apr. 2022, doi: 10.1007/s00170-022-08737-9.
- [2] R. Zhu, G. Yang, Z. Fang, J. Dai, C.-Y. Chen, G. Zhang, and C. Zhang, "Hybrid orientation/force control for robotic polishing with a 2R1T forcecontrolled end-effector," *Int. J. Adv. Manuf. Technol.*, vol. 121, nos. 3–4, pp. 2279–2290, Jul. 2022, doi: 10.1007/s00170-022-09407-6.
- [3] T. Czimmermann, M. Chiurazzi, M. Milazzo, S. Roccella, M. Barbieri, P. Dario, C. M. Oddo, and G. Ciuti, "An autonomous robotic platform for manipulation and inspection of metallic surfaces in Industry 4.0," *IEEE Trans. Autom. Sci. Eng.*, vol. 19, no. 3, pp. 1691–1706, Jul. 2022, doi: 10.1109/TASE.2021.3122820.
- [4] Z. Wu, J. Shen, Y. Peng, and X. Wu, "Review on ultra-precision bonnet polishing technology," *Int. J. Adv. Manuf. Technol.*, vol. 121, nos. 5–6, pp. 2901–2921, Jul. 2022, doi: 10.1007/s00170-022-09501-9.
- [5] A. R. Ahmad, C.-Y. Lin, S. H. Shah, and Y.-S. Cheng, "Design of a compliant robotic end-effector tool for normal contact estimation," *IEEE Sensors J.*, vol. 23, no. 2, pp. 1515–1526, Jan. 2023, doi: 10.1109/JSEN.2022.3226492.
- [6] H. Xie, Q. Wang, S. K. Ong, A. Y. C. Nee, X. Zhou, and Z. Liao, "Automatic generation of interference-free and posture-smooth toolpath for robotic belt grinding of complex workpieces," *IEEE/ASME Trans. Mechatronics*, vol. 28, no. 1, pp. 518–530, Feb. 2023, doi: 10.1109/TMECH.2022.3205852.
- [7] I. El Makrini, G. Mathijssen, S. Verhaegen, T. Verstraten, and B. Vanderborght, "A virtual element-based postural optimization method for improved ergonomics during human–robot collaboration," *IEEE Trans. Autom. Sci. Eng.*, vol. 19, no. 3, pp. 1772–1783, Jul. 2022, doi: 10.1109/TASE.2022.3147702.
- [8] Y. Zhou, C.-Y. Chen, G. Yang, and Y. Li, "A sampling-based motion assignment strategy with multi-performance optimization for macro-micro robotic system," *IEEE Robot. Autom. Lett.*, vol. 7, no. 4, pp. 11649–11656, Oct. 2022, doi: 10.1109/LRA.2022.3204867.
- [9] R. N. A. Algburi, H. Gao, and Z. Al-Huda, "Improvement of an industrial robotic flaw detection system," *IEEE Trans. Autom. Sci. Eng.*, vol. 19, no. 4, pp. 3953–3967, Oct. 2022, doi: 10.1109/TASE.2022.3141248.
- [10] K. Zhou, S. Wang, R. Zhou, and B. Wang, "Admittance control design and system testing of industrial robot polishing operation," *Proc. Inst. Mech. Eng., B, J. Eng. Manuf.*, vol. 237, no. 10, pp. 1538–1552, Aug. 2023, doi: 10.1177/09544054221136513.
- [11] Z. Li, L. Sun, J. Liu, Y. Qin, N. Sun, and L. Zhou, "Proxy-based sliding mode force control for compliant grinding via diagonal recurrent neural network and Prandtl–Ishlinskii hysteresis compensation model," *Actua*tors, vol. 13, no. 3, p. 83, Feb. 2024, doi: 10.3390/act13030083.
- [12] H. Ochoa and R. Cortesão, "Impedance control architecture for robotic-assisted mold polishing based on human demonstration," *IEEE Trans. Ind. Electron.*, vol. 69, no. 4, pp. 3822–3830, Apr. 2022, doi: 10.1109/TIE.2021.3073310.
- [13] C. Fan, C. Xue, L. Zhang, K. Wang, Q. Wang, Y. Gao, and L. Lu, "Design and control of the belt-polishing tool system for the blisk finishing process," *Mech. Sci.*, vol. 12, no. 1, pp. 237–248, Feb. 2021, doi: 10.5194/ms-12-237-2021.
- [14] S. Lloyd, R. A. Irani, and M. Ahmadi, "Improved accuracy and contact stability in robotic contouring with simultaneous registration and machining," *IEEE Trans. Control Syst. Technol.*, vol. 32, no. 4, pp. 1140–1155, Jul. 2024, doi: 10.1109/TCST.2023.3348749.
- [15] R. Pan, C. Hu, J. Fan, Z. Wang, X. Huang, and F. Lu, "Study on optimization of the dynamic performance of the robot bonnet polishing system," Int. J. Adv. Manuf. Technol., vol. 125, nos. 9–10, pp. 4561–4577, Apr. 2023, doi: 10.1007/s00170-023-10998-x.
- [16] Y. Ding, J. Zhao, and X. Min, "Impedance control and parameter optimization of surface polishing robot based on reinforcement learning," *Proc. Inst. Mech. Eng., B, J. Eng. Manuf.*, vol. 237, nos. 1–2, pp. 216–228, Jan. 2023, doi: 10.1177/09544054221100004.
- [17] C. Wu, K. Guo, and J. Sun, "Dual PID adaptive variable impedance constant force control for grinding robot," *Appl. Sci.*, vol. 13, no. 21, pp. 11635–11656, Oct. 2023, doi: 10.3390/app132111635.
- [18] C. Hebbi and H. R. Mamatha, "Comprehensive dataset building and recognition of isolated handwritten Kannada characters using machine learning models," *Artif. Intell. Appl.*, vol. 1, no. 3, pp. 179–190, Apr. 2023, doi: 10.47852/bonviewaia3202624.

- [19] X. Zhou, K. Sun, J. Wang, J. Zhao, C. Feng, Y. Yang, and W. Zhou, "Computer vision enabled building digital twin using building information model," *IEEE Trans. Ind. Informat.*, vol. 19, no. 3, pp. 2684–2692, Mar. 2023. doi: 10.1109/TII.2022.3190366.
- [20] L. Meng, Y. Li, H. Zhou, and Q. Wang, "A hybrid calibration method for the binocular omnidirectional vision system," *IEEE Sensors J.*, vol. 22, no. 8, pp. 8059–8070, Apr. 2022, doi: 10.1109/JSEN.2022.3158268.
- [21] B. Coifman and L. Li, "A new method for validating and generating vehicle trajectories from stationary video cameras," *IEEE Trans. Intell. Transp. Syst.*, vol. 23, no. 9, pp. 16227–16236, Sep. 2022, doi: 10.1109/TITS.2022.3149277.
- [22] Y. Xie, L. Deng, T. Sun, Y. Fu, J. Li, X. Cui, H. Yin, S. Deng, J. Xiao, and B. Chen, "A4LiDARTag: Depth-based fiducial marker for extrinsic calibration of solid-state LiDAR and camera," *IEEE Robot. Autom. Lett.*, vol. 7, no. 3, pp. 6487–6494, Jul. 2022, doi: 10.1109/LRA.2022.3173033.
- [23] N. Saini, E. Bonetto, E. Price, A. Ahmad, and M. J. Black, "AirPose: Multiview fusion network for aerial 3D human pose and shape estimation," *IEEE Robot. Autom. Lett.*, vol. 7, no. 2, pp. 4805–4812, Apr. 2022, doi: 10.1109/LRA.2022.3145494.
- [24] X. Chen, Z. Wang, Q. Hua, W.-L. Shang, Q. Luo, and K. Yu, "AI-empowered speed extraction via port-like videos for vehicular trajectory analysis," *IEEE Trans. Intell. Transp. Syst.*, vol. 24, no. 4, pp. 4541–4552, Apr. 2023, doi: 10.1109/TITS.2022.3167650.
- [25] H. Huang, W. He, J. Wang, L. Zhang, and Q. Fu, "An all servo-driven bird-like flapping-wing aerial robot capable of autonomous flight," *IEEE/ASME Trans. Mechatronics*, vol. 27, no. 6, pp. 5484–5494, Dec. 2022, doi: 10.1109/TMECH.2022.3182418.
- [26] T. Xu, Z. Hao, C. Huang, J. Yu, L. Zhang, and X. Wu, "Multimodal locomotion control of needle-like microrobots assembled by ferromagnetic nanoparticles," *IEEE/ASME Trans. Mechatronics*, vol. 27, no. 6, pp. 4327–4338, Dec. 2022, doi: 10.1109/TMECH.2022.3155806.
- [27] F. Hou, J. Liu, K. Liu, P. Wang, G. Li, and S. Guo, "3-D-curved iontronic tactile sensor and denoising method for physical human–robot interactions," *IEEE Sensors J.*, vol. 23, no. 7, pp. 7667–7682, Apr. 2023, doi: 10.1109/JSEN.2023.3247834.
- [28] Y. Wang, A. Zahedi, Y. Zhao, and D. Zhang, "Extracting human-exoskeleton interaction torque for cable-driven upper-limb exoskeleton equipped with torque sensors," *IEEE/ASME Trans. Mechatronics*, vol. 27, no. 6, pp. 4269–4280, Dec. 2022, doi: 10.1109/TMECH.2022.3154087.
- [29] M. Gandolfi and M. Ceotto, "Molecular dynamics of artificially pair-decoupled systems: An accurate tool for investigating the importance of intramolecular couplings," *J. Chem. Theory Comput.*, vol. 19, no. 18, pp. 6093–6108, Sep. 2023, doi: 10.1021/acs.jctc.3c00553.
- [30] T. Li, F. Chen, Z. Zhao, Q. Pei, Y. Tan, and Z. Zhou, "Hybrid data-driven optimization design of a layered six-dimensional FBG force/moment sensor with gravity self-compensation for orthopedic surgery robot," *IEEE Trans. Ind. Electron.*, vol. 70, no. 8, pp. 8568–8579, Aug. 2023, doi: 10.1109/TIE.2022.3231257.



KAI LIU was born in Taixing, Jiangsu, in February 1988. He received the bachelor's degree in electrical engineering and automation and the master's degree in electrical engineering from China University of Mining and Technology, in June 2011 and June 2014, respectively.

During his student studies, he focused on power electronics technology, motor control, DSP, and machine vision. From September 2014 to May 2017, he worked as a Teaching Assistant at

Changzhou Vocational Institute of Mechatronic Technology, where he has been a Lecturer and a Professional Leader, since June 2017. He has published the key textbook "Machine Vision Technology and Applications" for Higher Education Institutions in Jiangsu Province, and Hosted the School Level Key Scientific and Technological Project "Design of Robot Dynamic Sorting System Based on Machine Vision."